Journal of Materials Chemistry A

ROYAL SOCIETY OF CHEMISTRY

PAPER

View Article Online
View Journal | View Issue

Cite this: J. Mater. Chem. A, 2025, 13, 25110

Exploiting S_2^{2-}/S^{2-} redox chemistry in pseudo-layered chain-structured titanium trisulfide cathodes for high-energy magnesium–lithium hybrid ion batteries†

Pengcheng Jing, [a] Atsushi Inoishi, [b] Eiichi Kobayashi,[c] Chengcheng Zhao,[a] Yisong Han,[d] Peng Ren,[e] Isaac Abrahams [e] and Duncan H. Gregory *[a]

Magnesium–lithium hybrid ion batteries (MLIBs) offer a compelling alternative to conventional lithium-ion batteries (LIBs) due to their enhanced safety, abundant magnesium resources, and high theoretical capacities. However, the lack of high-capacity cathode materials has hindered their widespread application. In this study, we explore the potential of pseudo-layered titanium trisulfide (TiS_3) as a novel cathode material for MLIBs. TiS_3 features a chain-like structure with both S_2^{2-} and S^{2-} species, providing abundant ion storage sites and leveraging an S_2^{2-}/S^{2-} redox mechanism. The TiS_3 electrode achieves a maximum reversible capacity of *ca.* 381 mA h g^{-1}, corresponding to a high energy density of *ca.* 483 W h kg^{-1}, along with robust rate capability (*ca.* 213 and 138 mA h g^{-1} at 1000 mA g^{-1}, 2.69C, and 3000 mA h g^{-1}, 8.06C, respectively) and extended cycling stability (*ca.* 160 mA h g^{-1} after 1700 cycles at 2.69C). Mechanistic insights obtained *via ex situ* X-ray absorption spectroscopy (XAS) confirm the S_2^{2-}/S^{2-} redox mechanism, while *in operando* powder X-ray diffraction (PXRD) reveals phase transitions linked to intercalation-induced changes in local structure. This work underscores the promise of anionic redox chemistry in inorganic intercalation compounds and offers a new pathway for designing high-performance cathode materials for next-generation MLIBs and beyond.

Received 15th April 2025
Accepted 26th June 2025

DOI: 10.1039/d5ta02988k

rsc.li/materials-a

Introduction

Magnesium-ion batteries (MIBs) have emerged as promising next-generation energy storage systems due to their inherent advantages, including enhanced safety, abundant magnesium resources, high theoretical anode capacities, and suitable magnesium anode reduction potential.[1–3] Despite these merits, the divalent nature of Mg^{2+} ions poses challenges, such as strong electrostatic interactions and poor magnesium ion diffusion kinetics, which hinder the development of high-performance cathode materials.[1,4] To overcome these limitations, magnesium–lithium hybrid ion batteries (MLIBs) have been developed by incorporating lithium salts into magnesium-based electrolytes.[5] This hybrid system combines the favourable kinetics of Li^+ intercalation and diffusion with the dendrite-free magnesium stripping/plating at the Mg anode,[6–12] making MLIBs a promising alternative to address the capacity and reversibility limitations of conventional MIB cathodes.

Cathode materials with cationic redox mechanisms have been extensively studied in MLIBs. For instance, intercalation-type layered VS_2 was reported to exhibit a reversible capacity of *ca.* 181 mA h g^{-1} at a current density of 50 mA g^{-1}, attributed to the V^{4+}/V^{3+} redox reaction.[13,14] Similarly, TiS_2 was shown to deliver a stable cycling capacity of 220 mA h g^{-1} at a current density of 24 mA g^{-1}, driven by the Ti^{4+}/Ti^{3+} redox couple.[15] Additional cation-centred intercalation materials, including VO_2, TiO_2, MoS_2, and $Li_3V_2(PO_4)_3$,[16–19] have shown potential for MLIB energy storage applications. However, solely relying on cationic redox mechanisms often limits the achievable capacities, prompting exploration into alternative redox chemistries.

Anionic redox reactions in inorganic intercalation compounds have garnered increasing attention due to their potential to deliver higher capacities. In lithium ion batteries (LIBs), lithium-rich layered oxides, such as $Li_2Ru_{1-y}Sn_yO_3$ and $Li_{1.20}Mn_{0.54}Co_{0.13}Ni_{0.13}O_2$,[20,21] exhibit reversible $(O_2)^{n-}/O^{2-}$ redox behaviour, enabling capacities beyond those achievable with cationic redox. However, these oxide materials are prone to

[a]WestCHEM, School of Chemistry, Joseph Black Building, University of Glasgow, Glasgow, G12 8QQ, UK. E-mail: Duncan.Gregory@glasgow.ac.uk
[b]Institute for Materials Chemistry and Engineering, Kyushu University, Kasuga-koen 6-1, Kasuga, Fukuoka, 816-8580, Japan
[c]Kyushu Synchrotron Light Research Center, 8-7 Yayoigaoka, Tosu, Saga, 841-0005, Japan
[d]Department of Physics, University of Warwick, Coventry, CV4 7AL, UK
[e]Department of Chemistry, Queen Mary University of London, Mile End Road, London, E1 4NS, UK

† Electronic supplementary information (ESI) available. See DOI: https://doi.org/10.1039/d5ta02988k

oxygen release, which poses safety risks like thermal runaway.[22,23] Transition metal sulfides (TMSs) offer a potentially safer and more reliable alternative for anionic redox reactions. For example, layered $Li_{1.13}Ti_{0.57}Fe_{0.3}S_2$ was reported to demonstrate a S^{n-}/S^{2-} redox ($n < 2$) redox mechanism in LIBs supporting capacities up to 245 mA h g^{-1}.[24] Similarly, S_2^{2-}/S^{2-} redox behaviour was observed in layered iron sulfide Li_2FeS_2, evidenced by X-ray absorption spectroscopic (XAS) characterisation of the S K-edge. Although these materials have not been employed in MLIBs, other compounds directly containing S_2^{2-} have been increasingly explored and shown promising electrochemical performance. Pyrite-type disulfides, such as FeS_2, were explored in MLIBs and exhibited initial capacities as high as *ca.* 800 mA h g^{-1}.[25] However, these materials undergo a conversion-type reaction, resulting in significant structural degradation and accumulation of converted products to form "dead" electrode regions, causing rapid capacity fading upon extended cycling. Intercalation-type TMSs with S_2^{2-} anions are promising candidates to achieve high capacities while maintaining stable long-term cycling. Chain-structured TMSs containing disulfide species (S_2^{2-}) provide a unique opportunity to exploit anionic redox mechanisms without destructive conversion reactions. Vanadium pentasulfide (VS_4), featuring S_2^{2-} anions coordinated with vanadium in a tetragonal-antiprismatic structure,[26] has been extensively studied in MLIBs, demonstrating reversible capacities ranging from 300 mA h g^{-1} to 400 mA h g^{-1} *via* a co-intercalation mechanism.[27–29] Beyond VS_4, other chain-like disulfide-containing TMSs remain underexplored, highlighting the need for further investigation into these materials.

In this study, we report, for the first time, the application of a pseudo-layered titanium trisulfide (TiS_3) as a novel cathode material for MLIBs. TiS_3 adopts a chain-like structure containing both S_2^{2-} and S^{2-}, offering abundant sites for ion storage. The TiS_3 electrode achieves a maximum reversible capacity of *ca.* 381 mA h g^{-1}, corresponding to a high energy density of *ca.* 483 W h kg^{-1}. Additionally, the electrode exhibits robust rate capability (*ca.* 213 and 138 mA h g^{-1} at 2.69C and 8.06C, respectively) and long cycling life (*ca.* 160 mA h g^{-1} over 1700 cycles at 2.69C). Mechanistic studies using *ex situ* and *in operando* techniques reveal S_2^{2-}/S^{2-} redox chemistry and phase transitions likely associated with intercalation-induced changes in local structure. This work provides valuable insights into the use of anionic redox chemistry in inorganic intercalation compounds, paving the way for the development of high-performance cathode materials for next-generation MLIBs and beyond.

Results and discussion

The synthesis of the TiS_3 compound involved a simple physical vapour trasport (PVT) method, as detailed in the experimental section. Phase purity was confirmed by PXRD (Fig. S1a†), where the diffraction pattern matched the monoclinic TiS_3 phase (PDF – 15–0783; space group $P2_1/m$).[30] Notably, the (00*l*) and (*h*0*l*) diffraction peaks exhibit disproportionate intensities, suggesting preferred orientation of the TiS_3 crystallites. Rietveld refinement was performed to obtain accurate structural

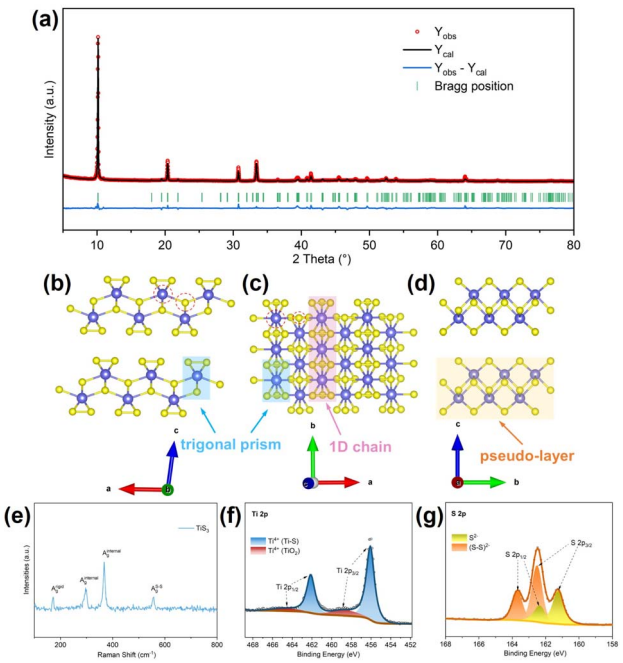

Fig. 1 (a) Fitted PXRD profile for the as-made TiS_3. Crystallographic illustration of the structure of TiS_3 viewed along the (b) *b*-axis, (c) near *c*-axis, and (d) *a*-axis as visualised by Vesta software.[33] (e) Raman spectrum of the as-synthesised TiS_3 compound. XPS high-resolution spectra in the: (f) Ti 2p and (g) S 2p regions for TiS_3.

parameters (Fig. 1a, Tables S1 and S2†). The refined lattice parameters were determined as $a = 4.9677(7)$ Å, $b = 3.4000(2)$ Å, $c = 8.7973(3)$ Å, and $\beta = 97.73°(1)$, consistent with values previously reported in the literature.[31,32] The monoclinic crystal structure of TiS_3 is illustrated in Fig. 1b–d. The [TiS_6] trigonal prisms (light blue bands; Fig. 1b and c) are bonded and extend along the *b*-axis *via* S–Ti–S bridges that exhibit polar covalent bonding, resulting in the formation of infinite 1D chains (light pink band; Fig. 1c). These chains are arranged together along the *a*-axis into pseudo-layers, connected by weak interchain Ti–S interactions (red dashed lines) with partial covalent character (light yellow band; Fig. 1d). Ultimately, the pseudo-layers stack along the *c*-axis *via* weak van der Waals (vdWs) forces, resulting in the production of bulk crystal of TiS_3. The interlayer spacing $d_{(001)}$ of TiS_3, derived from the Rietveld refinement, is *ca.* 0.87 nm.

Raman spectroscopy further verified the structural integrity of the as-synthesised TiS_3 (Fig. 1e). Four prominent peaks are observed at *ca.* 173 cm^{-1}, 299 cm^{-1}, 367 cm^{-1}, and 557 cm^{-1}, in good agreement with observed values in the literature.[34] Fig. S1b† provides a structural illustration of the relevant vibrational modes overlaid on the TiS_3 crystal lattice. The peak at *ca.* 173 cm^{-1} corresponds to out-of-plane rigid vibration (A_g^{rigid}) of inter and intrachain T–S bonds in two adjacent 1D chains of a pseudo-layer along the *c*-axis. Peaks at *ca.* 299 cm^{-1} and 367 cm^{-1} are attributed to two categories of in-plane $A_g^{internal}$ vibrations. The difference between them lies in the vibrational directions among the three components, namely, Ti atoms, bridging sulfur, and paired sulfur atoms, across

a double [TiS_6] trigonal prism. Additionally, the high-frequency peak at 557 cm^{-1} is associated with in-plane vibrations of intrachain S–S bonds (A_g^{S-S}) with minor contributions from out-of-plane interchain Ti–S vibrations. XPS analysis provided insights into the valence states of Ti and S in as-synthesised TiS_3. In the high-resolution Ti 2p spectrum (Fig. 1f), two pairs of doublet peaks are seen. The first pair of peaks, located at *ca.* 456.0 eV and 462.1 eV, correspond to the Ti $2p_{3/2}$ and Ti $2p_{1/2}$ transitions, respectively, representing the characteristic binding energies of Ti^{4+} in TiS_3.[35] The weak doublet peaks at *ca.* 458.6 eV and 464.6 eV correspond to the typical binding energies for Ti^{4+} in TiO_2, attributable to surface oxidation of TiS_3 during handling in air.[36,37] With respect to the high-resolution S 2p spectrum (Fig. 1g), two sets of doublet peaks can be discerned. The peaks at *ca.* 161.2 eV (S $2p_{3/2}$) and *ca.* 162.4 eV (S $2p_{1/2}$) are assigned to S^{2-} species in TiS_3, while those at *ca.* 162.5 eV and 163.7 eV are identified as S_2^{2-} species.[35]

The morphology and composition of the as-synthesised TiS_3 were characterised using SEM-EDS and TEM. As shown in Fig. 2a and b, SEM images at low- and high-magnifications reveal platelet- or rod-like particles with aspect ratios ranging from 2 to 15 (length of 1–15 μm and lateral dimension of 0.5–3 μm). These particles loosely stack and can be easily separated *via* sonication in common solvents such as ethanol and acetone. The SEM image and corresponding EDS elemental maps of Ti, S, and O are presented in Fig. 2c. It is evident that the distributions of Ti and S are uniform across the TiS_3 particles, while the presence of oxygen may be attributed to the surface oxidation, as also observed by XPS. The corresponding EDS spectrum (Fig. 2d) gives an S/Ti atomic ratio of 3.01 ± 0.06, consistent with the expected stoichiometry of TiS_3. The TEM image (Fig. 2e) further reveals the micro-to-nano-sized TiS_3 platelets or rods, interspersed with smaller and thinner fragments. HRTEM imaging (Fig. 2f) shows well-defined lattice fringes with *d* spacings of 0.49(1) and 0.34(2) nm, corresponding to the (100) and (010) crystal planes of monoclinic TiS_3, respectively.

The electrochemical behaviour of TiS_3 electrodes was investigated using galvanostatic (dis)charge cycling and CV measurements. As depicted in Fig. S2a,† the CV profiles of the TiS_3 electrode in MIBs exhibit minimal redox activity, indicating a limited capacity for Mg^{2+} accommodation. In contrast, pronounced redox peaks are observed for the TiS_3 electrode in MLIBs (Fig. 3a). Specifically, a pair of distinct redox peaks at *ca.* 0.87 V (cathodic) and 2.00 V (anodic) emerge during the first cycle. Over subsequent cycles, these peaks shift closer together and broaden with reduced intensities, indicative of reduced polarisation for the redox reaction within the electrode. Notably, the greater shift of the cathodic peak, commonly observed for trichalcogenide electrodes in MLIBs, MIB, and

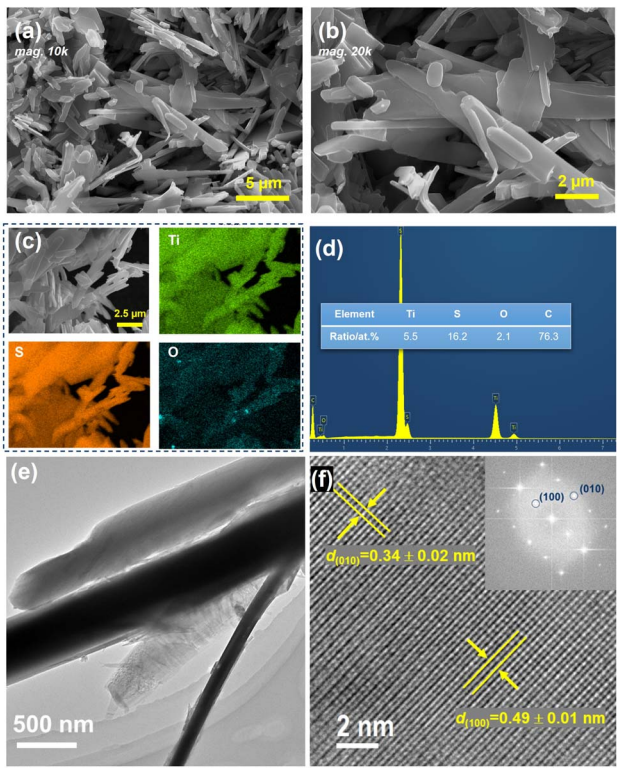

Fig. 2 Electron microscopic studies of the as-synthesised TiS_3: (a) low-magnification SEM image (×10k) and (b) corresponding higher-magnification (×20k) SEM image. (c) SEM image and corresponding EDS element maps for Ti, S, and O, respectively, and (d) corresponding EDS spectrum with an embedded table providing percentages of Ti, S, O, and C. (e) TEM and (f) HRTEM images. Inset (f) is the fast Fourier transformation (FFT) of the image.

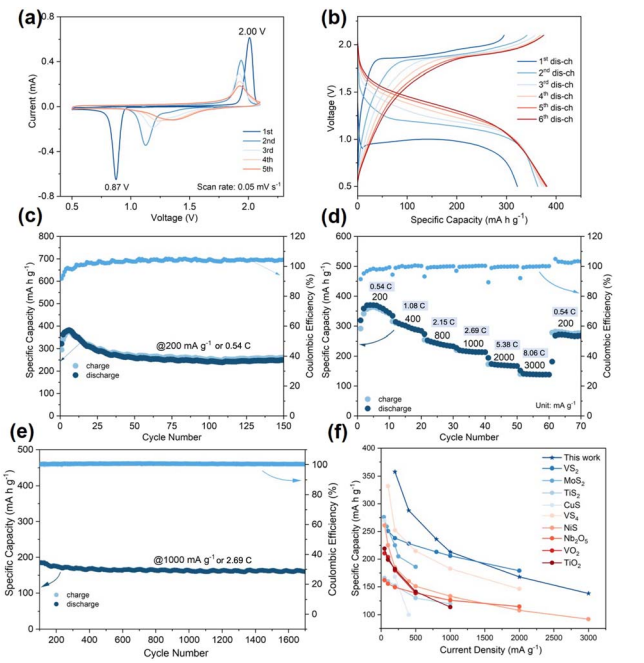

Fig. 3 Electrochemical performance evaluations of the TiS_3 electrodes in (−)Mg|LiAPC|TiS_3(+) MLIB cells. (a) Initial five CV cycles at a scan rate of 0.05 mV s^{-1} between 0.5–2.1 V. (b) Initial six (dis)charge curves at a current density of 200 mA g^{-1} between 0.5–2.1 V. (c) Cycling performance at 200 mA g^{-1}. (d) Rate performance at various current densities. (e) Long-term cycling performance at a high current density of 1000 mA g^{-1} (plotted from the 100th cycle). (f) Comparison of rate capabilities between TiS_3 and previously reported MLIB electrode materials.

even LIBs, suggests enhanced ion intercalation and cathodic processes. The (dis)charge profiles further corroborate these observations. As shown in Fig. S2b,† the TiS_3 electrode delivers negligible capacities (*ca.* 1.5 mA h g^{-1}) in MIBs at a current density of 200 mA g^{-1}. However, when measured in MLIBs, the same electrode demonstrates substantial capacities, reaching *ca.* 381 mA h g^{-1} after the initial cycles (Fig. 3b). This capacity sightly exceeds the theoretical faradaic limit of 372 mA h g^{-1}, which may be attributed to several factors. First, additional charge storage arising from non-faradaic pseudo capacitance or electric double-layer (EDL) capacitance is likely, possibly induced by *in situ* electrochemical nanosizing of bulk particles and the subsequent increase in surface area (see Fig. 4). The continuous exposure of fresh electrode surface likely promotes side reactions with the electrolyte, which may also contribute to the excess capacity observed. Second, the discharge cut-off voltage employed may have been marginally lower than the threshold required for complete two-electron transfer, but not sufficiently low to initiate a third-electron faradaic process, thereby allowing a small surplus in capacity. Third, the experimental deviation, estimated at ±5 mA h g^{-1} with an average measured capacity of 377 mA h g^{-1}, may also account for the minor excess observed. The cycling of the TiS_3 electrode in a Li-ion half-cell configuration yields an activated capacity of 376 mA h g^{-1} (Fig. S3†), also providing as a baseline reference for the theoretical capacity discussed above. Upon closer examination of the discharge profiles, the discharge plateau present during the first cycle shifts to higher voltage in the subsequent cycles and evolves into a slope-like shape. This behaviour aligns with the shifting and broadening of peaks observed in the CV curves.

The cycling performance of the TiS_3 electrode in MLIBs was further evaluated. As illustrated in Fig. 3c, the electrode undergoes an initial "activation" process to achieve a maximum reversible capacity of *ca.* 381 mA h g^{-1} and subsequent maintaining of stable cycling capacities up to *ca.* 250 mA h g^{-1} over 150 cycles. The observed capacity fade during cycling will be discussed in the coming sections centred around Fig. 4, 5 and 7. The C-rate capability (1C = 372 mA h g^{-1}) and long-term cycling stability of the TiS_3 electrodes in MLIBs were also investigated. As depicted in Fig. 3d, the TiS_3 electrode delivers capacities of *ca.* 358 mA h g^{-1}, 288 mA h g^{-1}, 236 mA h g^{-1}, 213 mA h g^{-1}, 168 mA h g^{-1}, and 138 mA h g^{-1} as the current density gradually escalates from 200 mA g^{-1} (0.54C) to 400 mA g^{-1} (1.08C), 800 mA g^{-1} (2.15C), 1000 mA g^{-1} (2.69C), 2000 mA g^{-1} (5.38C), and 3000 mA g^{-1} (8.06C), respectively. Fig. S4† provides the (dis) charge curves under different current densities. The long-term cycling stability of the electrode is remarkable, with a capacity of *ca.* 160 mA h g^{-1} retained after 1700 cycles (Fig. 3e, plotted from the 100th cycle after initial "activation" and capacity adjustment). Fig. 3f compares the rate capability of the TiS_3 electrode with other reported MLIB cathodes, showcasing its superior performance.[16,29,38–44] This highlights the potential of TiS_3 as a high-performance cathode material for next-generation MLIBs.

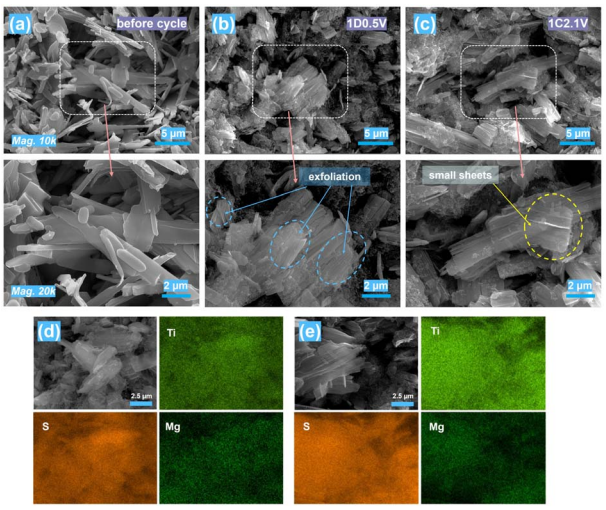

Fig. 4 Low- (above) and high-magnification (below) SEM images of the TiS_3 electrodes cycled in MLIBs at a current density of 200 mA g^{-1} in the: (a) uncycled, (b) first discharged (1D0.5V), and (c) first charged (1C2.1V) states. SEM-EDS element maps in (d) 1D0.5V and (e) 1C2.1V states.

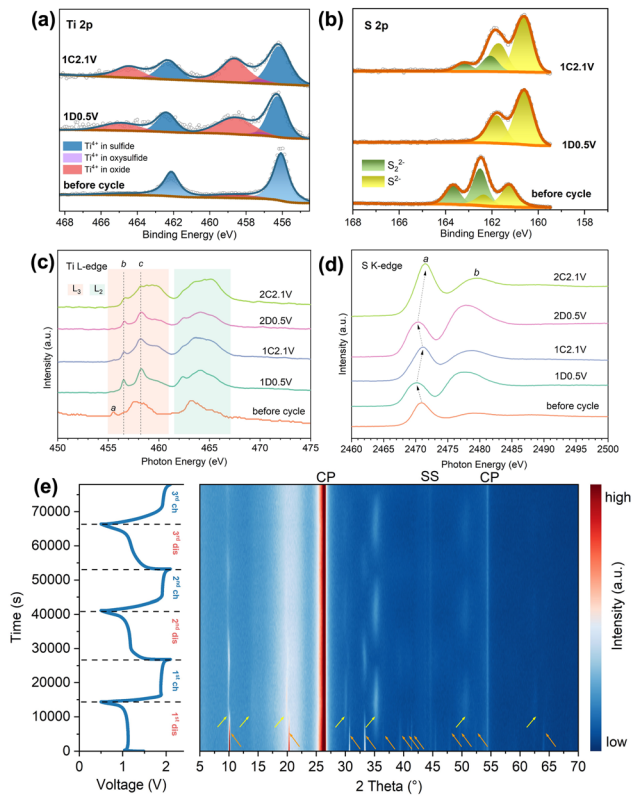

Fig. 5 High-resolution (a) Ti 2p and (b) S 2p XPS spectra in the TiS_3 electrodes at various discharge and charge states. XAS spectra of the (c) Ti L-edge and (d) S K-edge for the TiS_3 electrodes at various (dis) charge states. (e) Initial three cycles of (dis)charge curves (left) and corresponding contour plot of *in operando* PXRD patterns (right) for TiS_3 electrode in MLIBs at a current density of 100 mA g^{-1}. The diffraction peaks for TiS_3 and phase 1 are highlighted by orange and yellow arrows, respectively. The diffraction peaks of the carbon paper current collector (CP) and from the stainless-steel coin cell case (SS) are indicated in the graph.

The morphology and compositional evolution of the TiS_3 electrode at various (dis)charge states were examined using SEM-EDS. Low- and high-magnification SEM images of uncycled TiS_3 particles reveal smooth, relatively featureless surfaces (Fig. 4a). However, after the first discharge, exfoliation and delamination are observed, propagating from the surface into the bulk of the platelet-like particles, indicative of volume expansion due to intercalation of mobile species (Li^+ and/or Mg^{2+}). Typically, as shown in Fig. 4b, the exfoliation process results in the formation of smaller, ribbon-like crystals with high aspect ratios distributed sparsely on and around the bulk particles (circled in blue dashed lines). This behaviour aligns with analogous phenomena observed for trichalcogenides such as TiS_3, HfS_3, and ZrS_3 when chemically lithiated with Li^+ ions.[45,46] The interchain bonding in TiS_3 is partially characterised by weak vdWs forces, facilitating cleavage along the chain direction. For instance, theoretical cleavage energies for TiS_3 have been calculated as 0.320, 0.714, 0.716, and 0.815 J m^{-2} along the (001), (101), (10$\bar{1}$), and (100) planes, respectively, compared to significantly higher value of 2.706 J m^{-2} along the (010) planes.[46] This indicates that Li^+ intercalation-induced stress may result in the expansion of $[TiS_6]_n$ chains, causing the exfoliation of bulk TiS_3 platelets into small ribbon-like crystals. After the first charge, further exfoliation of the bulk particles is observed (Fig. 4c). Notably, thin sheets composed of interconnected ribbons, possibly detached from the parent particles, were frequently decorated with smaller dispersed particles (circled in yellow dashed lines). Examination of the electrode morphology after extended cycling (*e.g.* the 35th discharge/charge cycle; Fig. S5†) reveals pronounced exfoliation, yielding numerous small platelet-like crystals. Many of these fragments often cluster around larger particles and appear prone to detachment from the conductive matrix. Progressive exfoliation increases the electrode–electrolyte interfacial area, thereby exacerbating parasitic surface reactions and contributing to the observed capacity loss during cycling. Furthermore, the detached or partially isolated particles likely exhibit poor electrical conductivity and may become coated with electron-blocking solid electrolyte interphase (SEI) layers. Such particles are rendered electrochemical inactive, particularly under high current densities (*e.g.* 1000 mA g^{-1} or 2.69C), when rapid charge transfer and efficient ionic transport are required. The accumulation of these electrochemically inactive regions thus contributes to the capacity fading observed in the cycling tests. The EDS element maps and spectra for Ti, S, and Mg at various (dis)charge states are shown in Fig. 4d, e and S6.† It can be observed that the distributions of Ti, S, and Mg are uniform across the particles at different (dis)charge states, with minimal contrast variation in Mg between discharged and charged samples. The Mg : Ti atomic ratios are small in magnitude but remain comparable between the discharged and charged states (Table S3†). To distinguish between surface-bound and host-lattice-trapped Mg, XPS depth profiling with Ar^+ etching was conducted, revealing Li^+ as the dominant species from surface to bulk (Fig. S7†). However, Mg signals, although very weak, persist throughout the depth, indicating that Mg^{2+} ions are likely trapped within the host lattice. This finding is consistent with the similarity of galvanostatic (dis) charge profiles for TiS_3 in MLIBs and LIBs systems (Fig. S3b†). The electrodes after extended (35 cycles) cycling were also investigated by EDS (Fig. S8 and Table S4†). The concentrations of Mg and Cl are comparably large and increase/reduce simultaneously at discharge/charge states, suggesting that magnesium ion storage (likely in the form of $Mg_xCl_y^+$, a mixture of Mg^{2+}, $MgCl^+$, $Mg_2Cl_3^+$, or other Mg–Cl cationic complexes[7]) becomes partially reversible over extended cycles. This reversibility may be attributed to cycling-induced improvements, such as nano sizing and structure adjustments, which facilitate intercalation and diffusion of larger cations. For the discharged electrode after the 35th cycle, an Mg : Ti atomic ratio of ~0.5 is observed. To further study the main charge carrier after extended cycles, the TiS_3 electrode was first activated in LiAPC electrolyte and then allowed to cycle in APC electrolyte. The activated electrode exhibits a stable reversible magnesium ion storage capacity of around 155 mA h g^{-1} (Fig. S9†), accounting for 62% of the capacity in LiAPC electrolyte. This indicates that mixed magnesium species become the main charge carriers during prolonged cycling in LiAPC.

The oxidation states of Ti and S in TiS_3 electrodes in various (dis)charge states were analysed using XPS and XAS. In the high-resolution Ti 2p XPS spectra (Fig. 5a), peaks for Ti^{4+} in sulfide (*ca.* 456.1 eV and 462.2 eV) remain dominant across all states, accompanied by the presence of peaks for Ti^{4+} in oxide (*ca.* 458.6 eV and 464.8 eV) and oxysulfide (*ca.* 457.2 eV and 463.3 eV).[36] These findings suggest that Ti^{4+} in the TiS_3 electrodes is not reduced during discharging to form Li_2TiS_3 (1D0.5V). The presence of oxide and oxysulfide peaks is likely due to oxidation or hydrolysis of the highly air- and moisture-sensitive Li_2TiS_3 during electrode handling.[47] In contrast, S 2p spectra (Fig. 5b) indicate the complete reduction of S(–I) species (*ca.* 162.5 eV and 163.7 eV) to S(–II) (*ca.* 160.6 eV and 161.8 eV) upon discharge. The S 2p spectrum of the charged electrode shows partial recovery of S(–I) species, suggesting that some of the fully restored S(–I) species (observed in the following XAS analysis) on the electrode surface may be lost to oxidation or hydrolysis, as corroborated by the Ti 2p spectra.

XAS analysis supports the XPS findings, providing further insight into the oxidation states and coordination environments. Ti L-edge spectra (Fig. 5c) reveal two main edges: L_3 (454–461 eV) and L_2 (461–467 eV), associated with transitions from Ti 2p orbitals (Ti $2p_{3/2}$ and Ti $2p_{1/2}$) to unoccupied 3d orbitals ($2p^5$ $3d^1$).[35] The spectrum of the uncycled sample features two broad, overlapping L_3- and L_2-edge peaks, along with a small pre-edge peak ("a"), arising from multiplet core-hole and 3d electron interactions.[48] The L_2-edge peaks are typically broader and less resolved than the L_3-edge peaks, primarily due to the shorter lifetime of the $2p_{1/2}$ core hole and the near-threshold Coster–Kronig decay.[49] Consequently, the analysis in the following discussion focuses primarily on the L_3-edge. Upon the first discharge (1D0.5V), the Ti Li_3-edge peaks become more distinct, showing pronounced splitting into t_{2g} and e_g states ("b" and "c", respectively), likely due to a change in Ti coordination from trigonal prismatic to octahedral symmetry, commonly observed in stable titanium

dichalcogenides, such as 1T TiS_2.[50] The b and c peaks are positioned at *ca.* 456.5 eV and 458.2 eV, which are higher in energy than the characteristic peak positions from Ti^{3+} states (typically at *ca*. 455.8 eV and 457.3 eV) observed in intercalated chalcogenides.[51] Instead, these values are consistent with the Ti^{4+} states reported in compounds such as $Li_{1.13}Ti_{0.57}Fe_{0.3}S_2$ and $BaTiS_3$.[24,52] This observation suggests that the Ti^{4+} oxidation state in the TiS_3 electrode remains unaltered upon discharge, in agreement with the XPS results and supporting the premise that titanium hardly participates in the redox process. After the first charge (1C2.1V), the Ti coordination geometry persists, with minimal changes in the Ti^{4+} state, suggesting irreversible local structural changes with lithium ion de-intercalation. The subsequent cycle resembles the first cycle, although high-energy features become more prominent, possibly due to structural degradation at high voltage caused by the corrosion effect of the Cl-containing LiAPC electrolyte. Turning to the S K-edge spectrum (Fig. 5d), there are two main features for the uncycled TiS_3. The high-resolution pre-edge feature observed at *ca.* 2470.9 eV (denoted as peak "a") is attributed to the S 1s → S 3p transition, with limited hybridisation with Ti 3d obitals.[35] The absence of distinct pre-edge peaks corresponding to S_2^{2-} and S^{2-} species has been previously explained by the predominance of S_2^{2-} species in TiS_3, with the S^{2-} signal assumed to be shifted upwards to an energy nearly coinciding with that of the two sulfur atoms in S_2^{2-}.[35] Additionally, the lack of a splitting feature in the S K-edge pre-peaks has been attributed to suppressed Ti–S d-p hybridisation in TiS_3.[35] These characteristics suggest that the redox activity is likely centred on the sulfur anions, rather than shared with titanium cations, which is consistent with the observed invariance of the Ti^{4+} state throughout the cycling. The weak, broad peak at around 2479.1 eV corresponds to transitions to higher energy states, such as S 1s to S 3p/Ti 4s, 3p, which involve the complete ejection of the core electron into the continuum.[35] For the spectra of cycled samples, peak a shifts to a lower energy of *ca.* 2470.1 eV during discharge, indicating an increase in the electron density around sulfur and a reduction in effective nuclear charge. This observation suggests the reduction of S_2^{2-} to S^{2-} anions. The singlet nature of the pre-edge profile is attributable to the lack of clear energetic separation among these S^{2-} species. Upon charging, this feature returns to higher energy, comparable to that of pristine TiS_3, reflecting the reversible oxidation of S^{2-} to S_2^{2-}. These findings confirm the reversible S_2^{2-}/S^{2-} redox mechanism in the TiS_3 electrode during cycling.

Structural changes of TiS_3 during cycling were investigated using *in operando* PXRD. As shown in Fig. 5e, the initial discharge process leads to the appearance of new peaks (yellow arrows) at *ca.* 9.9°, 14.4°, 19.9°, 30.0°, 35.3°, 49.1°, 50.6°, 62.5°, and 64.8°, and the progressive disappearance of peaks corresponding to TiS_3 (orange arrows). This indicates a phase transition to a new phase (Li_xTiS_3-like phase 1, $x \leq 2$), which exhibits obvious disparities with those of known monoclinic (electrochemically inactive) and cubic Li_2TiS_3 phases (Fig. S10a†). Notably, there are disproportional shifts of (001) and (002) peaks (from *ca*. 10.1° to *ca*. 9.9° and from 20.3° to 19.9°; Fig. S10b†), indicating lattice expansion along the *c*-axis by *ca.* 0.02 nm. This is attributable to changes in the local structure after Li^+ ions are intercalated, rather than to the size effect of Li^+ (0.74 Å) or Mg^{2+} (0.72 Å). After the breakage of S–S bonds in the $[TiS_6]_n$ chains, Ti coordination may change from trigonal prismatic to octahedral geometry (as suggested by the XAS analysis), as seen from the most stable Ti octahedral geometry in chalcogenides, such as 1T TiS_2.[53] In addition to this coordination change, the reduction of sulfur anions (*e.g.* S_2^{2-} to S^{2-}) during discharge can increase the effective ionic radius of the anion framework. Both effects – Ti coordination change and the formation of larger S^{2-} species – can contribute to a thickening of the pseudo-layers and corresponding expansion of the lattice along the *c*-axis. Upon charging, phase 1 peaks gradually diminish, accompanied by recovery of a poorly-crystalised TiS_3 phase. It is noteworthy that the (001) and (002) peaks of TiS_3 do not fully revert to their original positions (Fig. S10b†), suggesting incomplete structural recovery. This may be attributed to the trapping of a certain amount of Li^+ cations (and/or Mg^{2+}), as well as challenges in restoring the original local structure, including Ti coordination and the re-formation of partial S–S bonds. Although the S_2^{2-}/S^{2-} redox process is previously proposed to be reversible based on findings from the XAS characterisation, the observed partial structural irreversibility, plus the 10% capacity loss in the first cycle, suggests that part of this transformation may be irreversible in the whole electrode particles under the present electrochemical conditions. Subsequent cycles exhibit similar trends, except for the increasing poor crystallinity of the recovered TiS_3 phase and the more disordered pseudo-layer structure (relating to (001) and (002) peaks). It is worth noting that the absence of a well-defined reference structure for the lithiated phase, combined with the pronounced amorphisation observed upon cycling, present significant challenges to structural refinement. Future studies employing *in situ* synchrotron pair distribution function (PDF) analysis or advanced DFT-based modelling may yield deeper insights into the structural evolution of lithiated TiS_3.

Extended-cycle *in operando* PXRD patterns of the TiS_3 electrode (starting from the 45th fully charged state) reveal partial retention of phase 1 peaks (*e.g. ca.* 14.4°, 35.3°, and 50.6°), while TiS_3 peaks become negligible (Fig. S11†). Loss of long-range order in phase 1, likely due to pseudo-layer sliding and TiS_3 chain misfit, is evidenced by the absence of (00*l*) reflections at *ca*. 9.9°, 19.9°, and 30.0°. The diffraction peaks of this "transformed" phase 1 progressively shift to slightly lower angles during discharge cycles, while they return to their original positions after charging. This behaviour indicates $Li^+/Mg_xCl_y^+$ ion (supported by EDS results in extended cycles) intercalation/de-intercalation-driven lattice expansion and contraction.

The above PXRD analysis sheds light on the capacity fading following the initial capacity activation, from the perspective of structural irreversibility (*e.g.* local Ti coordination geometry and bulk-phase amorphisation), aside from the contributions from parasitic electrolyte reactions and the accumulation of detached, electrochemically less active sections of the material.

To elucidate the structural changes occurring in the TiS_3 electrode during initial and extended cycles, a hypothetical schematic is presented in Fig. 6. During the first discharge to

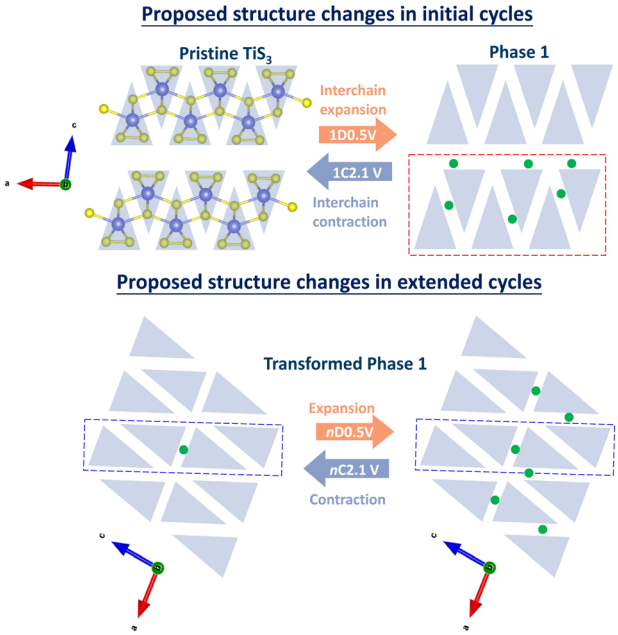

Fig. 6 A simplified schematic of hypothetical structural changes in TiS_3 during initial and extended cycles. The $[TiS_6]_n$ chains, extending along the *b*-axis, are simplified as light blue triangles. Intercalated Li^+/Mg^{2+} (or $Mg_xCl_y^+$) ions are depicted as green solid circles. The red dashed rectangle indicates the pseudo-layer of the host structure during the initial cycles, while the blue dashed rectangle represents the potential "pseudo-layer" or "slab" of the host structure ("transformed" phase 1) during extended cycling.

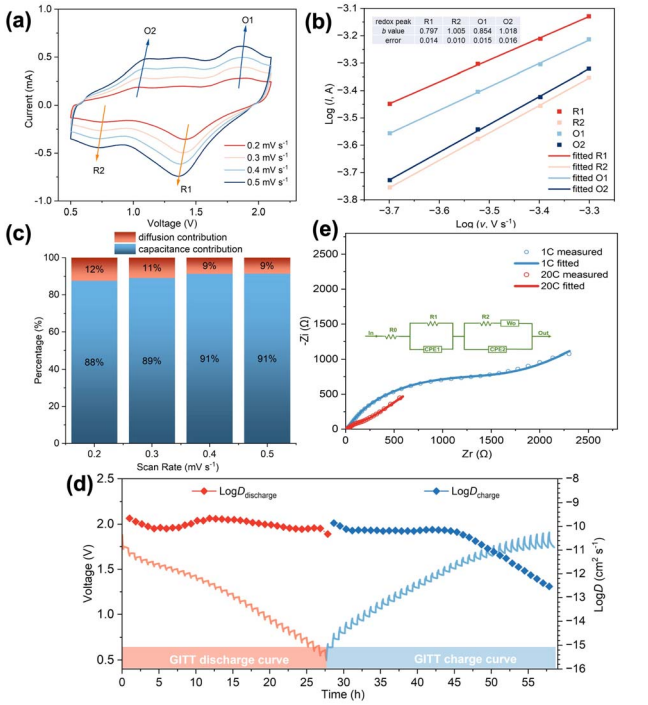

Fig. 7 Evaluations of the electrochemical properties for the TiS_3 electrodes: (a) CV curves at different scan rates of 0.2 mV s^{-1} (red), 0.3 mV s^{-1} (light red), 0.4 mV s^{-1} (light blue), and 0.5 mV s^{-1} (blue), respectively. (b) Plots of the measured and simulated Log oxidation (blue and light blue) and Log reduction (red and light red) peak currents against the Log of scan rates *v*. (c) Histogram representing the capacitative and diffusive percentage at different scan rates. (d) GITT discharge–charge curves measured at a current pulse of 50 mA g^{-1} and corresponding Log $D_{discharge}$ and Log D_{charge}. (e) Nyquist plots and respective fits of the cells containing TiS_3 electrodes at the 1st and 20th charged states.

0.5 V, phase 1 is formed, marked by an expansion of the interchain spaces, as evidenced by the appearance of a diffraction peak at 14.4° and additional peaks unrelated to the pseudo-layer structure. This expansion is attributed to the incorporation of Li^+ (and trace amounts of Mg^{2+}) ions and possible accompanying adjustments in the local structure. These adjustments include changes in Ti–S bond lengths, electrostatic interactions between adjacent $S^{2-}\cdots S^{2-}$ anions (these are formed from the cleavage of disulfide bonds), the size of the sulfur anion framework, and modifications in Ti coordination geometry. During charging, these changes partially reverse as Li^+ (and trace Mg^{2+}) ions are extracted from the host lattice. However, after prolonged and repeated ion (de-)intercalation cycles, the pseudo-layer structure (outlined by the red dashed rectangle) exhibits significant disorder. This is likely due to chain or pseudo-layer sliding along the *a*-axis or other possible directions, disrupting the long-range order of the crystal planes and leading to the eventual loss of diffraction signals. Consequently, during extended cycling, lattice expansion and contraction are hypothesised to occur primarily within the slab region (highlighted by the blue dashed rectangle) and the inter-slab spaces.

The electrochemical properties of the TiS_3 electrode were assessed using various approaches, including CV, GITT, and EIS. Initially, CV curves were collected at different scan rates of 0.2 mV s^{-1}, 0.3 mV s^{-1}, 0.4 mV s^{-1}, and 0.5 mV s^{-1} (Fig. 7a). The CV peak positions at these scan rates were extracted and subjected to linear fitting using eqn (S1) and (S2)†, as shown in Fig. 7b. The calculated b_R/b_O values for the two redox couples were $(0.797 \pm 0.014)/(0.854 \pm 0.015)$ and $(1.005 \pm 0.010)/(1.018 \pm 0.016)$, respectively. These results indicate that the R_1/O_1 redox couple involves mixed pseudo capacitative and diffusion-controlled processes, while the R_2/O_2 couple is predominantly capacitative. To quantify the contributions of capacitative and diffusive mechanisms, the CV current data and scan rates were linearly fitted using eqn (S3).† Fig. 7c shows the capacitive contributions to overall charge storage at scan rates of 0.2 mV s^{-1}, 0.3 mV s^{-1}, 0.4 mV s^{-1}, and 0.5 mV s^{-1} to be 88%, 89%, 91%, and 91%, respectively. These findings indicate that the measured capacities are not purely faradaic, but predominately capacitive in nature, likely resulting from the electrochemical nanosizing of the electrode materials. The persistence of redox peaks at both low and high scan rates, coupled with the ongoing structural expansion and contraction during cycling, suggests that the dominant capacitance arises from redox-driven (near-) surface intercalation or absorption, characteristic of pseudo capacitance. While EDL capacitance may also contribute, its role is likely minor, as the exfoliated electrode does not appear to exhibit sufficiently high surface area to support substantial EDL charge storage. Therefore, the charge storage mechanism

in the TiS_3 electrode is primarily governed by rapid (near) surface pseudo-capacitive processes, consistent with its observed high-rate performance and long cycling stability.

The GITT approach was used to investigate the $Li/Mg_xCl_y^+$ mixed ion diffusion kinetics in the TiS_3 electrode by calculating the diffusion coefficient (D) from the measured GITT curves, according to eqn (S4).† As shown in Fig. 7d, the D values during discharge range from 0.48×10^{-10} cm^2 s^{-1} to 2.20×10^{-10} cm^2 s^{-1}, while those during charge vary between 2.92×10^{-13} cm^2 s^{-1} to 1.40×10^{-10} cm^2 s^{-1}. The average discharge D of *ca.* 1.20×10^{-10} cm^2 s^{-1} indicates good $Li/Mg_xCl_y^+$ mixed ion diffusion in the host lattice. The decline in diffusion coefficients during charging to the maximum cut-off voltage can be attributed to the parasitic reactions caused by partial incompatibility between TiS_3 and the Cl-containing electrolyte, as evidenced by the discharge/charge coulombic efficiency (109%) much exceeding 100%. These parasitic reactions, such as electrolyte decomposition, electrode corrosion, and structural degradation, can be exacerbated under the low current densities and extended relaxation periods employed in GITT. The observed excessive (or irreversible) GITT charging capacity of 309 mA h g^{-1}, compared to a discharge capacity of 284 mA h g^{-1}, underscores these parasitic losses. Increasing the (dis)charge current density to 200 mA g^{-1} and 1000 mA g^{-1} mitigates these effects (Fig. 3c–e), consistent with previous reports for Mg-based systems with Cl-containing electrolytes.[43,54–56] Therefore, the D values at the high voltage stage during the charging process may not provide informative insights. Future studies will focus on halide-free electrolytes compatible with TiS_3 to reduce these parasitic reactions. While alternatives like glyme-based electrolytes using $Li[B(hfip_4)]$ and $Mg[B(hfip_4)]_2$ (where $[B(hfip)_4]^-$ is hexafluoroisopropyloxy borate anion) offer higher anodic stability beyond 2.2 V and are halide-free, their effectiveness in TiS_3 remains uncertain due to the instability of $[B(hfip)_4]^-$ anions at higher voltage,[57] as evidenced by the excessive coulombic efficiency of *ca.* 111% at 20 mA g^{-1} in TiS_2 studies.[58] Further development of robust, halide-free electrolytes is essential for enhancing TiS_3 electrode performance.

EIS was conducted to investigate the charge transfer resistance, interfacial properties, and ion diffusion at the electrode–electrolyte interface using (−)Mg|0.5 M LiCl/0.2 M APC|TiS_3(+) cells. Nyquist plots for the uncycled, first charged, and 20th charged states were fitted using a modified Randles equivalent circuit (Fig. S13† and 7e). The circuit consists of three components: (i) resistor R_0, representing the internal resistance; (ii) a combination of resistor and constant phase element in parallel (R_1 + CPE_1), associated with the solid-electrolyte-interphase (SEI); and (iii) an in-series pair of resistance (R_2) and a Warburg impedance (W_0), representing charge transfer and ion diffusion impedance, respectively, in parallel with a constant phase element (CPE_2). By analysing the measured and fitted curves alongside the key parameters derived from the simulation (Table S5†), the change in the electrochemical behaviour can be discerned. After the first cycle, R_1 decreases significantly to *ca.* 15 Ω and remains stable after 20 cycles, possibly due to the removal of passivation/oxidation layers and the establishment of a favourable SEI. Similarly, R_2 and W_0 drop from 25 601 Ω and 3077 Ω $s^{-0.5}$ in the uncycled state to *ca.* 1678 Ω and 953 Ω $s^{-0.5}$ after the first cycle, and further to 190 Ω and 271 Ω $s^{-0.5}$ after 20 cycles. These results suggest enhanced charge transfer and reduced $Li^+/Mg_xCl_y^+$ ion diffusion impedance, possibly due to *in situ* particle size reduction and removal of surface oxides during cycling.

Conclusions

This work explores the potential of PVT-synthesised, disulfide-containing, chain-like TiS_3 as a novel cathode material for MLIBs. This material exhibits substantial reversible capacities up to 381 mA h g^{-1} (*i.e.* 483 W h kg^{-1}), along with excellent rate capability (*ca.* 213 and 138 mA h g^{-1} at 2.69C and 8.06C, respectively) and long cycling life (*ca.* 160 mA h g^{-1} after 1700 cycles at 2.69C). Comprehensive mechanistic analysis confirms the S_2^{2-}/S^{2-} redox mechanism in the TiS_3 electrode, accompanied by phase transitions likely associated with intercalation-induced changes in local structure. The mobile ion storage mechanism is Li^+-dominated intercalation in initial cycles but evolves to co-intercalation in the extended cycling regime. This work provides valuable insights into the use of S_2^{2-}/S^{2-} redox chemistry in inorganic intercalation compounds for the development of high-performance cathode materials for next-generation MLIBs and beyond. Meanwhile, future work will aim to address the current lack of theoretical validation of the anionic redox mechanism. In particular, density functional theory (DFT) calculations could be employed to assess the thermodynamic stability of anionic species, redox potentials, and bond dissociation energies. Such efforts would help to deepen the understanding of sulfur-anion-driven multielectron redox processes in disulfide-containing chalcogenides.

Data availability

The data supporting this article have been included as part of the ESI.†

Conflicts of interest

There are no conflicts to declare.

Acknowledgements

DHG and PJ thank the University of Glasgow and the China Scholarship Council for a PhD studentship for PJ. The authors also thank the Warwick Analytical Sciences Centre (WASC) at the University of Warwick for access to its TEM instrument (JEOL 2100 Plus) housed within the Department of Physics, supported by funding from EPSRC under grant code EP/V007688/1. Thanks also to Dr Christopher Kelly (University of Glasgow) for assistance with XPS measurements. Acknowledgments are also extended to the Institute for Molecular Science for providing access to the BL2A beamline of the UVSOR Synchrotron Facility, supported under the IMS Program with grant code 24IMS6007; and to the SAGA Light Source for access

to the BL12 beamline with Proposal No. 126-2301103P and 148-2302125P.

Notes and references

1 P. Canepa, G. Sai Gautam, D. C. Hannah, R. Malik, M. Liu, K. G. Gallagher, K. A. Persson and G. Ceder, *Chem. Rev.*, 2017, **117**, 4287–4341.
2 F. Liu, T. Wang, X. Liu and L.-Z. Fan, *Adv. Energy Mater.*, 2021, **11**, 2000787.
3 Y. Liang, H. Dong, D. Aurbach and Y. Yao, *Nat. Energy*, 2020, **5**, 646–656.
4 M. Mao, T. Gao, S. Hou and C. Wang, *Chem. Soc. Rev.*, 2018, **47**, 8804–8841.
5 H. J. Chang, Y. Cheng, D. Choi, H. Dong, G. Li, J. Liu, V. L. Sprenkle and Y. Yao, *J. Mater. Res.*, 2016, **31**, 3125–3141.
6 D.-T. Nguyen, A. Y. S. Eng, R. Horia, Z. Sofer, A. D. Handoko, M.-F. Ng and Z. W. Seh, *Energy Storage Mater.*, 2022, **45**, 1120–1132.
7 O. Mizrahi, N. Amir, E. Pollak, O. Chusid, V. Marks, H. Gottlieb, L. Larush, E. Zinigrad and D. Aurbach, *J. Electrochem. Soc.*, 2008, **155**, A103.
8 D.-T. Nguyen, A. Y. S. Eng, M.-F. Ng, V. Kumar, Z. Sofer, A. D. Handoko, G. S. Subramanian and Z. W. Seh, *Cell Rep. Phys. Sci.*, 2020, **1**, 100265.
9 L. Yang, C. Yang, Y. Chen, Z. Pu, Z. Zhang, Y. Jie, X. Zheng, Y. Xiao, S. Jiao, Q. Li and D. Xu, *ACS Appl. Mater. Interfaces*, 2021, **13**, 30712–30721.
10 Y. Cheng, R. M. Stolley, K. S. Han, Y. Shao, B. W. Arey, N. M. Washton, K. T. Mueller, M. L. Helm, V. L. Sprenkle, J. Liu and G. Li, *Phys. Chem. Chem. Phys.*, 2015, **17**, 13307–13314.
11 S. He, J. Luo and T. L. Liu, *J. Mater. Chem. A*, 2017, **5**, 12718–12722.
12 J. Luo, Y. Bi, L. Zhang, X. Zhang and T. L. Liu, *Angew. Chem.*, 2019, **131**, 7041–7045.
13 R. Sun, C. Pei, J. Sheng, D. Wang, L. Wu, S. Liu, Q. An and L. Mai, *Energy Storage Mater.*, 2018, **12**, 61–68.
14 Y. Meng, Y. Zhao, D. Wang, D. Yang, Y. Gao, R. Lian, G. Chen and Y. Wei, *J. Mater. Chem. A*, 2018, **6**, 5782–5788.
15 H. D. Yoo, Y. Liang, Y. Li and Y. Yao, *ACS Appl. Mater. Interfaces*, 2015, **7**, 7001–7007.
16 C. Pei, F. Xiong, J. Sheng, Y. Yin, S. Tan, D. Wang, C. Han, Q. An and L. Mai, *ACS Appl. Mater. Interfaces*, 2017, **9**, 17060–17066.
17 S. Su, Y. NuLi, Z. Huang, Q. Miao, J. Yang and J. Wang, *ACS Appl. Mater. Interfaces*, 2016, **8**, 7111–7117.
18 X. Yu, G. Zhao, H. Huang, C. Liu, P. Lyu and N. Zhang, *Chem. Eng. J.*, 2022, **428**, 131214.
19 M. Rashad, H. Zhang, X. Li and H. Zhang, *J. Mater. Chem. A*, 2019, **7**, 9968–9976.
20 A. Grimaud, W. T. Hong, Y. Shao-Horn and J. M. Tarascon, *Nat. Mater.*, 2016, **15**, 121–126.
21 H. Koga, L. Croguennec, M. Ménétrier, K. Douhil, S. Belin, L. Bourgeois, E. Suard, F. Weill and C. Delmas, *J. Electrochem. Soc.*, 2013, **160**, A786.
22 H. Zhang, H. Liu, L. F. J. Piper, M. S. Whittingham and G. Zhou, *Chem. Rev.*, 2022, **122**, 5641–5681.
23 Y. Yang, D. Fang, A. Maleki, S. Kohzadi, Y. Liu, Y. Chen, R. Liu, G. Gao and J. Zhi, *ACS Appl. Energy Mater.*, 2021, **4**, 10713–10720.
24 S. Saha, G. Assat, M. T. Sougrati, D. Foix, H. Li, J. Vergnet, S. Turi, Y. Ha, W. Yang, J. Cabana, G. Rousse, A. M. Abakumov and J.-M. Tarascon, *Nat. Energy*, 2019, **4**, 977–987.
25 Y. Zhang, J. Xie, Y. Han and C. Li, *Adv. Funct. Mater.*, 2015, **25**, 7300–7308.
26 M. N. Kozlova, Y. V. Mironov, E. D. Grayfer, A. I. Smolentsev, V. I. Zaikovskii, N. A. Nebogatikova, T. Y. Podlipskaya and V. E. Fedorov, *Chem. – Eur. J.*, 2015, **21**, 4639–4645.
27 P. Jing, H. Lu, W. Yang, Y. Cao, B. Xu, W. Cai and Y. Deng, *Ionics*, 2020, **26**, 777–787.
28 Y. Wang, C. Wang, X. Yi, Y. Hu, L. Wang, L. Ma, G. Zhu, T. Chen and Z. Jin, *Energy Storage Mater.*, 2019, **23**, 741–748.
29 X. Zhang, X. Tu, Y. Liu, Y. Zhu, J. Zhang, J. Wang, R. Shi and L. Li, *ACS Appl. Mater. Interfaces*, 2023, **15**, 37442–37453.
30 O. Gorochov, A. Katty, N. Le Nagard, C. Levy-Clement and D. M. Schleich, *Mater. Res. Bull.*, 1983, **18**, 111–118.
31 Z. Tian, X. Guo, D. Wang, D. Sun, S. Zhang, K. Bu, W. Zhao and F. Huang, *Adv. Funct. Mater.*, 2020, **30**, 2001286.
32 S. Furuseth, L. Brattås, A. Kjekshus, A. Andresen and P. Fischer, *Acta Chem. Scand.*, 1975, **10**, 623–631.
33 K. Momma and F. Izumi, *J. Appl. Crystallogr.*, 2011, **44**, 1272–1276.
34 K. Wu, E. Torun, H. Sahin, B. Chen, X. Fan, A. Pant, D. Parsons Wright, T. Aoki, F. M. Peeters, E. Soignard and S. Tongay, *Nat. Commun.*, 2016, **7**, 12952.
35 M. E. Fleet, S. L. Harmer, X. Liu and H. W. Nesbitt, *Surf. Sci.*, 2005, **584**, 133–145.
36 D. Gonbeau, C. Guimon, G. Pfister-Guillouzo, A. Levasseur, G. Meunier and R. Dormoy, *Surf. Sci.*, 1991, **254**, 81–89.
37 S. Södergren, H. Siegbahn, H. Rensmo, H. Lindström, A. Hagfeldt and S.-E. Lindquist, *J. Phys. Chem. B*, 1997, **101**, 3087–3090.
38 C. Pei, Y. Yin, X. Liao, F. Xiong, Q. An, M. Jin, Y. Zhao and L. Mai, *J. Energy Chem.*, 2021, **58**, 586–592.
39 X. Fan, R. R. Gaddam, N. A. Kumar and X. S. Zhao, *Adv. Energy Mater.*, 2017, **7**, 1700317.
40 P. Jing, H. Lu, W. Yang and Y. Cao, *Electrochim. Acta*, 2020, **330**, 135263.
41 Y. Tang, D. Tao, Y. Cao and F. Xu, *Phys. Chem. Chem. Phys.*, 2023, **25**, 22497–22504.
42 Y. Ma, K. Shuai, L. Zhou, J. Wang and Q. Wang, *Dalton Trans.*, 2020, **49**, 15397–15403.
43 G. Zhu, G. Xia, H. Pan and X. Yu, *Adv. Sci.*, 2022, **9**, 2106107.
44 Y. Meng, D. Wang, Y. Wei, K. Zhu, Y. Zhao, X. Bian, F. Du, B. Liu, Y. Gao and G. Chen, *J. Power Sources*, 2017, **346**, 134–142.
45 R. R. Chianelli and M. B. Dines, *Inorg. Chem.*, 1975, **14**, 2417–2421.
46 Y. Ōnuki, R. Inada, S. Tanuma, S. Yamanaka and H. Kamimura, *Solid State Ionics*, 1983, **11**, 195–201.

47 Y. Hu, Z. Sun, Z. Zhang, S. Liu, F. He, Y. Liu, Z. Zhuang and F. Liu, *Adv. Energy Mater.*, 2023, **13**, 2202756.
48 J. P. Crocombette and F. Jollet, *J. Phys.: Condens. Matter*, 1996, **8**, 5253.
49 F. Lin, Y. Liu, X. Yu, L. Cheng, A. Singer, O. G. Shpyrko, H. L. Xin, N. Tamura, C. Tian, T.-C. Weng, X.-Q. Yang, Y. S. Meng, D. Nordlund, W. Yang and M. M. Doeff, *Chem. Rev.*, 2017, **117**, 13123–13186.
50 Y. G. Yu and N. L. Ross, *J. Phys.: Condens. Matter*, 2011, **23**, 055401.
51 A. S. Shkvarin, Y. M. Yarmoshenko, A. I. Merentsov, Y. M. Zhukov, A. A. Titov, E. G. Shkvarina and A. N. Titov, *Phys. Chem. Chem. Phys.*, 2017, **19**, 4500–4506.
52 B. Zhao, M. S. B. Hoque, G. Y. Jung, H. Mei, S. Singh, G. Ren, M. Milich, Q. Zhao, N. Wang, H. Chen, S. Niu, S.-J. Lee, C.-T. Kuo, J.-S. Lee, J. A. Tomko, H. Wang, M. A. Kats, R. Mishra, P. E. Hopkins and J. Ravichandran, *Chem. Mater.*, 2022, **34**, 5680–5689.
53 D. W. Murphy and F. A. Trumbore, *J. Electrochem. Soc.*, 1976, **123**, 960.
54 R. Jiang, B. Liu, C. Du, M. Jin, X. Liu, X. Ma, Y. Zhu, M. Zou and C. Cao, *Chem. Eng. J.*, 2024, **488**, 150487.
55 Q. Zhang, Y. Hu, J. Wang and F. Pan, *J. Phys. Chem. C*, 2021, **125**, 19673–19681.
56 Q. Zhang, Y. Hu, J. Wang and F. Pan, *J. Magnesium Alloys*, 2023, **11**, 192–200.
57 T. Pavčnik, M. Lozinšek, K. Pirnat, A. Vizintin, T. Mandai, D. Aurbach, R. Dominko and J. Bitenc, *ACS Appl. Mater. Interfaces*, 2022, **14**, 26766–26774.
58 A. Roy, M. Sotoudeh, S. Dinda, Y. Tang, C. Kübel, A. Groß, Z. Zhao-Karger, M. Fichtner and Z. Li, *Nat. Commun.*, 2024, **15**, 492.